aerospace

MDPI

Article

Computational Study of Hybrid Propeller Configurations

Mingtai Chen *, Tianming Liu, Jack Edwards and Tiegang Fang

Department of Mechanical and Aerospace Engineering, North Carolina State University, 1840 Entrepreneur Drive, Raleigh, NC 27695, USA; tliu28@ncsu.edu (T.L.); jredward@ncsu.edu (J.E.); tfang2@ncsu.edu (T.F.)
* Correspondence: mchen33@ncsu.edu; Tel.: +1-919-515-8737

Abstract

This study presents the first computational investigation of hybrid propeller configurations that combine toroidal and conventional blade geometries. Using Delayed Detached Eddy Simulation (DDES) with the Shear Stress Transport (SST) $k-\omega$ model for flow analysis and the Ffowcs Williams and Hawkings (FW–H) formulation for aeroacoustic prediction, five hybrid propeller designs were evaluated: a baseline model and four variants with modified loop-element spacing. The results show that the V-Gap-S configuration achieves the highest figure of merit (FM), producing over 10% improvement in propeller performance relative to the baseline, while also exhibiting the lowest turbulence kinetic energy (TKE) levels across multiple radial planes. Aeroacoustic analysis reveals quadrupole-like directivity for primary tonal noise, primarily driven by blade tip–vortex interactions, with primary tonal noise strongly correlated with thrust. Broadband noise and overall sound pressure level (OASPL) exhibited dipole-like patterns, influenced by propeller torque and FM, respectively. Comparisons of surface pressure, vorticity, and time derivatives of acoustic pressure further elucidate the mechanisms linking blade spacing to aerodynamic loading and noise generation. The results demonstrate that aerodynamic performance and aeroacoustics are strongly coupled and that meaningful noise reduction claims require performance conditions to be matched.

Keywords: hybrid propeller; toroidal blade; DDES; aeroacoustics; turbulence flow

1. Introduction

Recently, the concept of urban air mobility (UAM) has gained significant attention. In the near future, highly automated UAM drones operating at lower altitudes within urban and suburban areas are expected to revolutionize intra-city transportation. However, the anticipated increase in urban air traffic could lead to various challenges, particularly noise pollution. As these drones become more prevalent in areas populated by people and communities, the impact of noise must be carefully considered during the design process [1]. The Federal Aviation Administration (FAA) and the European Union Aviation Safety Agency (EASA) are likely to impose stringent noise regulations on UAM drones in the coming years.

In this context, advances in fabrication, navigation, control, and power storage systems have enabled the development of a wide range of drones for UAM operations. These vehicles are increasingly capable of performing complex missions, ranging from surveillance and remote inspection to product delivery [2,3]. Unfortunately, the use of propellers in UAM drones exacerbates concerns about noise generation [4,5]. Researchers have explored various noise reduction strategies for propellers. Typically, those strategies are divided into

Check for updates

Academic Editor: Sujin Bureerat

Received: 22 December 2025
Revised: 8 January 2026
Accepted: 13 January 2026
Published: 15 January 2026

Copyright: © 2026 by the authors. Licensee MDPI, Basel, Switzerland. This article is an open access article distributed under the terms and conditions of the Creative Commons Attribution (CC BY) license.

two categories: passive and active flow control. To mitigate this issue, researchers have explored a range of noise reduction strategies, typically categorized into passive and active flow control methods. Passive approaches include the use of uneven blade spacing to suppress tonal noise [6], leading-edge boundary layer trips to reduce broadband noise under lightly loaded conditions [7], and serrated blade edges—both leading and trailing—to attenuate overall noise levels [8–10]. More recently, microfiber coatings composed of fibrous structures have been applied to propeller surfaces as a passive noise treatment [11]. However, as noted by Hasegawa and Sakaue [11], these studies often focus solely on noise reduction, neglecting aerodynamic performance. In contrast, Chen et al. [12] advocates for a balanced evaluation of both acoustic and aerodynamic characteristics, proposing a propeller trade-off index to guide design decisions.

Recently, the Massachusetts Institute of Technology (MIT) released a design patent for toroidal propellers, suggesting that this new type of propeller could reduce noise while maintaining the performance of conventional designs [13]. Following discussions with the inventor and the MIT patent office, interest in toroidal propellers has grown, with several companies and hobbyists eager to explore the technology, although commercialization remains ongoing. In the academic community, toroidal propellers have attracted growing attention in recent studies [14–22]. Nevertheless, comprehensive data on their performance and the aerodynamic mechanisms underpinning potential noise reduction remain limited. Moreover, as reported in Chen et al. [23], aerodynamic interference between the leading and trailing blades within a single toroidal loop can negatively impact performance, resulting in inferior efficiency compared to conventional commercial designs.

Regarding noise mitigation during the propagation phase, ducted propellers have been proposed. For instance, Malgoezar et al. [24] experimentally investigated how a rigid duct influences propeller noise radiation. However, if not properly designed, a duct can exacerbate noise levels. To address this, Guo et al. [25] proposed a liner duct system incorporating optimal sound-absorbing materials. In vertical flight configurations—where the propeller functions as a rotor—far-field noise signatures generated by rotor–wing interaction can be suppressed using active flow control techniques such as blowing at the plane of the wing, as demonstrated in Chen et al. [26].

Despite these developments, no existing studies have explored hybrid propellers that combine toroidal and conventional blade geometries. This work presents a numerical investigation of such a hybrid configuration, consisting of two blades that are half toroidal and half conventional. Four propeller variants derived from a baseline are designed to provide additional insights. Propeller performance, flow-fields, and aeroacoustic characteristics are obtained through numerical simulations and compared across the different designs. The ultimate goal is to identify the optimal hybrid geometry and provide some guidance for future hybrid propeller development.

2. Numerical Methods

2.1. Flow Modeling

The Delayed Detached Eddy Simulation (DDES) approach was chosen to simulate the flow, with the Shear Stress Transport (SST) $k-\omega$ model employed for turbulence modeling. The governing equations for the incompressible flow [27] are

$$\frac{\partial u_i}{\partial t} + \frac{\partial (u_i u_j)}{\partial x_j} = -\frac{1}{\rho}\frac{\partial p}{\partial x_i} + \frac{\partial}{\partial x_j}[(\nu + \nu_t)\frac{\partial u_i}{\partial x_j}], \quad (1)$$

$$\frac{\partial u_i}{\partial x_i} = 0. \quad (2)$$

The turbulent eddy viscosity ν_t is modified via DDES switching:

$$\nu_t = \rho \frac{a_1 k}{max(a_1\omega, SF_2)}, \tag{3}$$

where the relevant functions and terms are defined as

$$SF_2 = \sqrt{2S_{ij}S_{ij}} \quad and \quad S_{ij} = \frac{1}{2}(\frac{\partial u_i}{\partial x_j} + \frac{\partial u_j}{\partial x_i}). \tag{4}$$

Here, ρ is the density, u_i and u_j are the velocity components, p is the pressure, ν is the molecular viscosity, k is turbulent kinetic energy (TKE), ω is the specific dissipation rate, and S_{ij} is the strain-rate tensor. Default values of the constants are used, i.e., a_1 = 0.31, C_{DES} (Inner) = 0.78, C_{DES} (Outer) = 0.61, C_{d1} = 20, α^*_∞ = 1, α_∞ = 0.52, β^*_∞ = 1, β_i (Inner) = 0.075, and β_i (Outer) = 0.0828.

DDES combines the strengths of Reynolds-Averaged Navier–Stokes (RANS) and Large Eddy Simulation (LES) methods: the boundary layer is handled by RANS, while regions with significant flow separation are resolved using LES. Consequently, near-wall turbulence is approximated rather than fully resolved, allowing for a coarser mesh near solid surfaces and reducing the demand for fine-grid resolution.

The DDES model, detailed by Spalart et al. [28], is an adaptation of the original DES97 model through the introduction of a shielding function f_d that prevents premature switching to LES mode within the boundary layer. This limiter is defined in Equation (5):

$$f_d = 1 - \tanh([8r_d]^3), \tag{5}$$

where

$$r_d = \frac{\nu_t + \nu}{\omega d^2 \sqrt{S_{ij}S_{ij}}}. \tag{6}$$

Here, d is the wall distance. While Equations (5) and (6) were orignally developed for the Spalart-Allmaras (SA) DES model, the DDES implementation introduces a modified DES length scale $\tilde{d}$, defined in Equation (7):

$$\tilde{d} = d - f_d \max(0, d - C^{\mathrm{Outer}}_{\mathrm{DES}}\Delta). \tag{7}$$

In this formulation, $\tilde{d}$ depends on the grid size $\Delta = \max(\Delta x, \Delta y, \Delta z)$ and the eddy-visosity field through the f_d limiter.

The SST $k-\omega$ turbulence model, originally developed by Menter [29], governs turbulence in the boundary layer and is defined by the transport equations for k and ω, as presented in Equations (8) and (9):

$$\frac{\partial}{\partial t}(\rho k) + \frac{\partial}{\partial x_i}(\rho k u_i) = \frac{\partial}{\partial x_i}(\Gamma_k \frac{\partial k}{\partial x_j}) + \tilde{G}_k - Y_k + S_k, \tag{8}$$

$$\frac{\partial}{\partial t}(\rho \omega) + \frac{\partial}{\partial x_i}(\rho \omega u_i) = \frac{\partial}{\partial x_i}(\Gamma_\omega \frac{\partial \omega}{\partial x_j}) + G_\omega - Y_\omega + D_\omega + S_\omega. \tag{9}$$

Here, Γ_k and Γ_ω represent the effective diffusivity of k and ω, respectively. Y_k and Y_ω denote the dissipation of k and ω due to turbulence, while S_k and S_ω represent user-defined terms. $\tilde{G}_k$ represents the generation of turbulence kinetic energy due to mean velocity gradients, G_ω is the generation of ω, and D_ω is the cross-diffusion term.

2.2. Acoustics Computation

Acoustic predictions were conducted using the Ffowcs Williams and Hawkings (FW–H) acoustic analogy, formulated as

$$\frac{1}{c_0^2}\frac{\partial^2 p'}{\partial^2 t} - \nabla^2 p' = \frac{\partial^2}{\partial x \partial y}[T_{ij}H(f)] - \frac{\partial}{\partial x_i}[P_{ij}n_j + \rho u_i(u_n - v_n)]\delta(f) + \frac{\partial}{\partial t}[\rho_0 v_n + \rho(u_n - v_n)]\delta(f). \quad (10)$$

In this equation, p' represents the acoustic pressure, c_0 is the ambient speed of sound, ρ_0 is the ambient density, and v is the moving velocity of the data surface. The subscript n denotes the local normal term of the data surface. T_{ij} and P_{ij} correspond to the Lighthill stress tensor and the compressive stress tensor, respectively, while $H(f)$ and $\delta(f)$ are the Heaviside and Dirac delta functions. This formulation, as implemented in Zhi et al. [30], is consistent with the original approach of of Williams and Hawkings [31].

The FW–H solution includes contributions from quadrupole sources (e.g., turbulence-related noise), dipole sources (e.g., surface force-related noise), and monopole sources (e.g., mass fluctuation-related noise). In this study, quadrupole and monopole contributions were neglected due to the relatively low Reynolds number (Re), leaving dipole sources—primarily associated with unsteady aerodynamic forces on the propeller surfaces (e.g., pressure fluctuations)—as the dominant noise contributors.

All propeller surfaces were treated as FW–H integration surfaces for sound generation. Specifically, using DDES data from the final 20 propeller revolutions, transient acoustic fields were computed via the built-in FW–H acoustic model in ANSYS Fluent. The resulting acoustic pressure time series at selected receiver locations were post-processed using Fast Fourier Transform (FFT) to obtain sound pressure spectra.

In the transient simulations, the time step (Δt) was determined using Equation (11) to ensure sufficient temporal resolution for the maximum frequency of interest. A value of set to Δt = 8.33 $\times 10^{-5}$ seconds was used, and the total simulation time was one seconds:

$$\Delta t \leq \frac{1}{2 * freq}, \quad (11)$$

where $freq$ denotes the maximum frequency of interest.

3. Propeller Geometry

To numerically investigate the hybrid propeller, a base configuration is modeled as shown in Figure 1a,b. This design features a single blade that combines two elements: one half is a toroidal propeller, while the other half is a conventional propeller. Key specifications of both the toroidal and conventional components are detailed in Chen et al. [12,23].

To further examine the influence of geometric variations, four additional hybrid propeller variants are developed. Relative to the base configuration, two variants introduce changes to the loop elements in the horizontal direction—one with a large gap (Figure 1c) and the other with a small gap (Figure 1e)—designated as H-Gap-L and H-Gap-S, respectively. The other two variants modify the loop elements in the vertical direction: one with a large gap (Figure 1d) and one with a small gap (Figure 1f), referred to as V-Gap-L and V-Gap-S, respectively. While the primary geometric modification is applied in either the horizontal or vertical direction, minor secondary changes in the orthogonal direction may also occur.

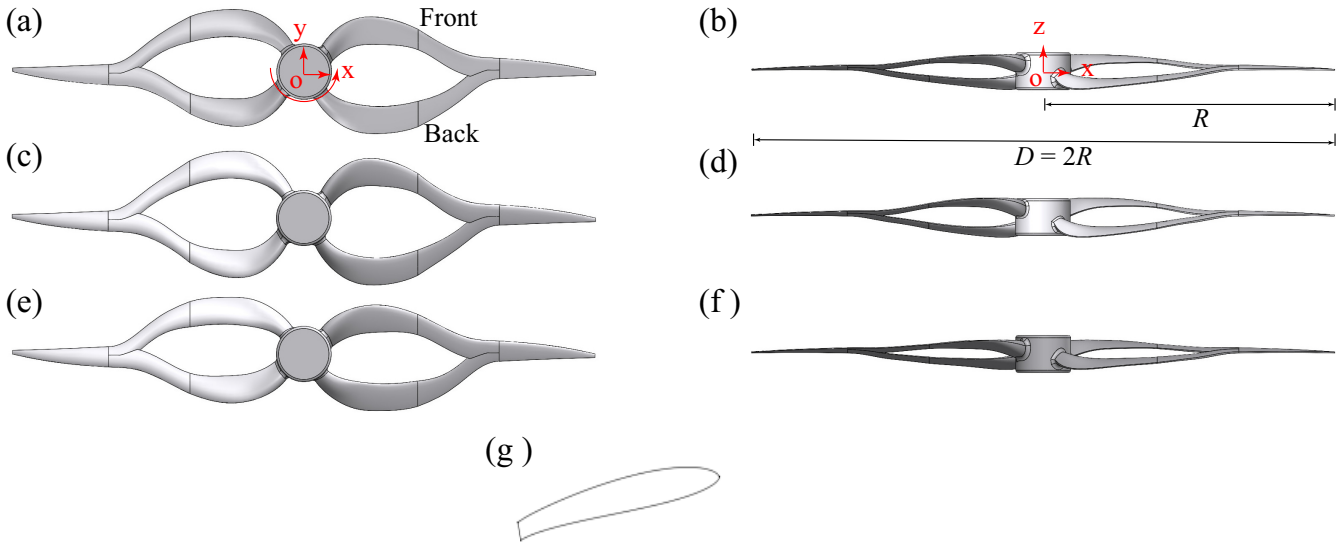


Figure 1. Visual comparison of five hybrid propeller geometries: (**a**) base-top view, (**b**) base-side view, (**c**) H-Gap-L, (**d**) V-Gap-L, (**e**) H-Gap-S, (**f**) V-Gap-S, and (**g**) baseline airfoil (not to scale).

All five hybrid propeller configurations have a diameter (D) of 10 inches and consist of two equivalent blades employing the same baseline airfoil (Figure 1g). The geometries are not optimized using design algorithms; such optimization is beyond the scope of the present study. In this study, the term front blade refers to the blade segment first encountering the rotational inflow (as shown in Figure 1a), followed by back blade, which spans from the propeller hub to approximately $0.50R$. From $0.50R$ to the blade tip, both the pitch angle and blade geometry remain constant. In the view presented in Figure 1b, front blade is positioned at a higher elevation than back blade.

4. Computational Setup

4.1. Domain

Numerical simulations were carried out in ANSYS Fluent (Version 21.2), a commercial Computational Fluid Dynamics (CFD) software. A velocity inlet boundary condition with a magnitude of 0.1 m/s was applied at the inlet, and a pressure outlet was used to define the end of the computational domain, as illustrated in Figure 2. To model the rotation of the hybrid propeller, a small rotating domain with a diameter of $1.1D$ and a depth of $0.2D$ was included within the stationary domain in meshing motion. The stationary domain is cylindrical with dimensions of $12D$ by $30D$ (diameter by length). The height from the center of the propeller to the inlet is $10D$ and to the outlet is $20D$. To capture the propeller wake more accurately, a refinement region is introduced: it extends from $1D$ above the propeller center to $8D$ below it and maintains a constant diameter of $2D$.

4.2. Grid

The computational domain was discretized utilizing an unstructured, polyhydral mesh generated with the meshing module in ANSYS Fluent. A refinement region was included around the rotating domain to improve resolution in the propeller wake, as shown in Figure 3a. Figure 3b presents the grid near the propeller model in the xz-plane. Inflation layers, illustrated in Figure 3c, were applied along the toroidal propeller surfaces to enhance boundary layer resolution—a critical factor for accurately capturing near-wall flow characteristics—alongside appropriate face sizing. This setup included ten layers with a growth (transition) ratio of 0.15 and an initial layer height of 0.01 mm, resulting in a y^+ value below 1 for the first layer above the propeller surfaces. The final mesh consisted

of approximately 17 million cells and was applied consistently across all five propeller configurations analyzed in this study. A grid-independence study is not included, as the mesh strategy is informed by prior validated simulations of conventional and toroidal propellers with the same diameter [12,23]. In those studies, numerical predictions of thrust and torque were compared with experimental measurements, demonstrating that meshes with significantly fewer cells already provided close agreement with experiments within 10% of error. The finer mesh employed in the present work is therefore considered sufficient for accurately predicting propeller performance while providing enhanced resolution of vortical structures and unsteady flow features.

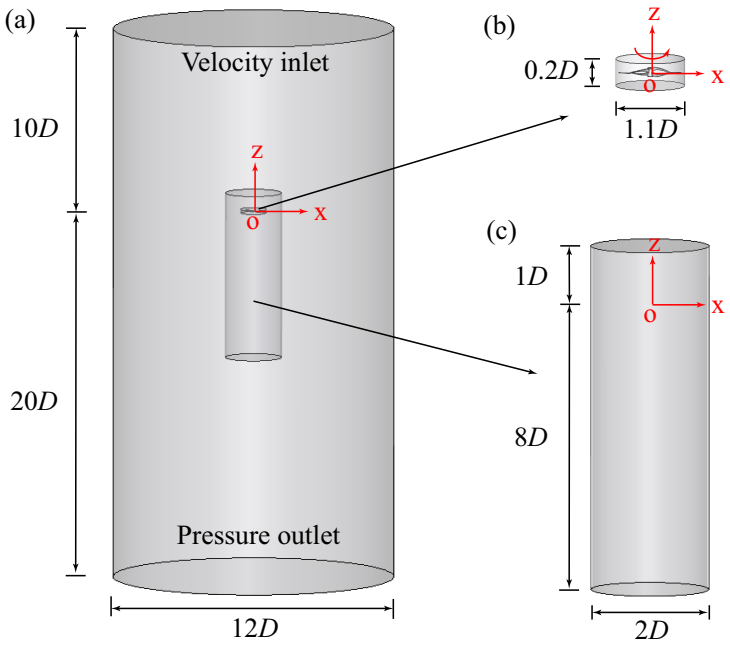


Figure 2. Presentation of simulation domains in ANSYS Fluent: (**a**) stationary domain, (**b**) rotating domain, and (**c**) refinement region.

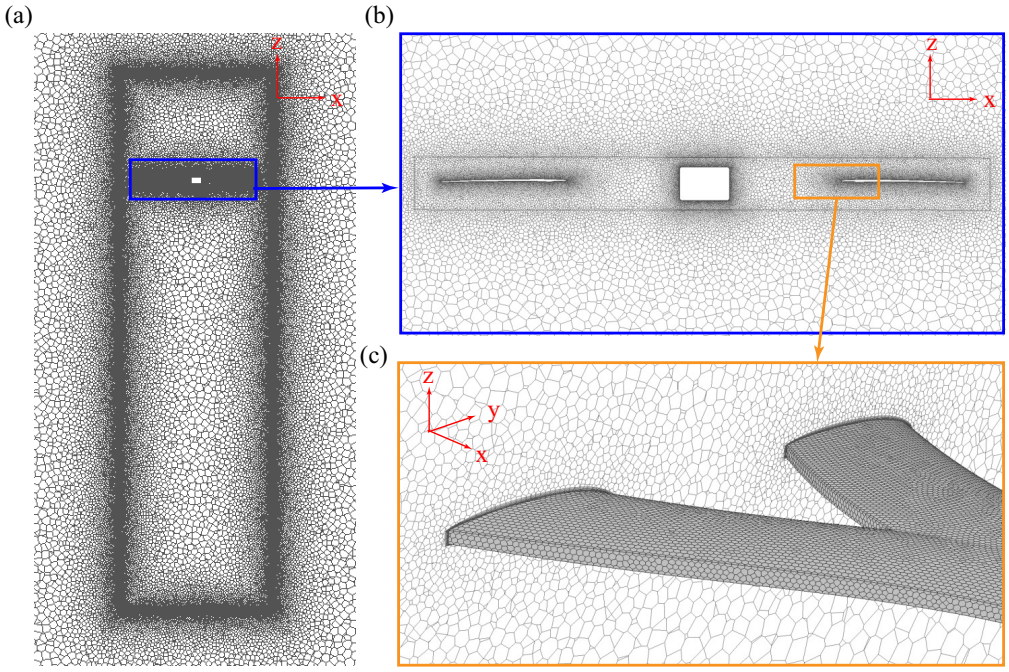


Figure 3. (**a**) Grid of the refinement region, (**b**) grid around the propeller model, (**c**) near-wall grids of the base configuration.

4.3. Solver

The pressure-based coupled algorithm was employed to resolve the pressure–velocity coupling, enhancing numerical stability and accelerating convergence in the transient flow simulation. Temporal discretization was carried out using a bounded second-order implicit scheme, which provides both stability and second-order accuracy for unsteady simulations.

The spatial discretization schemes were selected to ensure a balance between accuracy and numerical stability. The gradient was computed using the least squares cell-based method, which offers robustness on unstructured meshes. The pressure term was discretized using a second-order scheme, while the momentum equations were handled with the bounded central differencing scheme, suitable for LES-like behavior in DDES.

The turbulence quantities, including k and ω, were discretized using the second-order upwind scheme, preserving accuracy in regions with steep gradients. The residual convergence criterion was set to 10^{-6} for all equations, and propeller thrust and torque were monitored during the simulations.

4.4. Data Processing

4.4.1. Aerodynamic Data Processing

Propeller thrust (T) and torque (Q) measurements were nondimensionalized using Equations (12) and (13) [32], where A_{disk} is the propeller disk area and U_{tip} is the tip speed:

$$C_T = \frac{T}{\rho A_{disk} U_{tip}^2}, \tag{12}$$

$$C_Q = \frac{Q}{\rho A_{disk} U_{tip}^2 R}. \tag{13}$$

Figure of merit (FM) is a measure of propeller performance and is defined as the ratio between the ideal power required to hover and the actual power required [33]:

$$\mathrm{FM} = \frac{C_T^{3/2}}{\sqrt{2} C_P} = \frac{C_T^{3/2}}{\sqrt{2} C_Q} < 1. \tag{14}$$

For clarification, using the above nondimensionalization method, C_P and C_Q are numerically equivalent.

4.4.2. Aeroacoustic Data Processing

To process the acoustic results from the computations, the methodology is described in detail by Chen et al. [34]. The key steps for aeroacoustic data processing are summarized as follows:

- Tonal noise: Frequencies obtained from FFT are normalized by the blade passing frequency (BPF), as defined in Equation (11). Tonal components are identified as peaks occurring at integer values of the normalized frequency, f^+. In this study, the analysis focuses on the primary tonal noise corresponding to $f^+ = 1$.
- Broadband noise: Noise peaks are removed using a built-in function in MATLAB 2021.
- Overall sound pressure level (OASPL): The noise levels are integrated over the entire frequency range.

$$f^+ = \frac{f}{\mathrm{BPF}} \tag{15}$$

The BPF is defined in Equation (16):

$$\mathrm{BPF} = \frac{N \cdot \Omega}{60}, \tag{16}$$

where N is the number of blades on the hybrid propeller (equal to 2 in this study), and Ω is the rotational speed in revolutions per minute (RPM).

5. Results

The numerical results presented in the following sections—covering propeller performance, aeroacoustics, blade surface pressure, turbulence intensity, flow streamlines, vorticity, and time derivative of acoustic pressure for comparison—were obtained at 3000 RPM for all five hybrid configurations.

5.1. Propeller Performance

Figure 4a compares thrust coefficient (C_T), torque coefficient (C_Q), and FM for the baseline propeller and four variants (H-Gap-L, H-Gap-S, V-Gap-L, and V-Gap-S) to evaluate the influence of blade spacing within a single loop element on hybrid propeller performance. Overall, the V-Gap-S configuration achieves a slightly greater than 10% improvement in FM relative to the baseline. This model produces the highest thrust while requiring the lowest torque. By contrast, increasing the spacing in either the horizontal or vertical direction does not significantly improve propeller performance. The H-Gap-S model provides the second-best performance improvement. It is hypothesized that large blade spacing increases the blade–air interaction area near the hub, where the local rotational speed is relatively low, thereby producing additional drag and turbulence. To support this interpretation, static pressure coefficient contours on the propeller surfaces are shown in Figure 4b, with the coefficient defined by Equation (17).

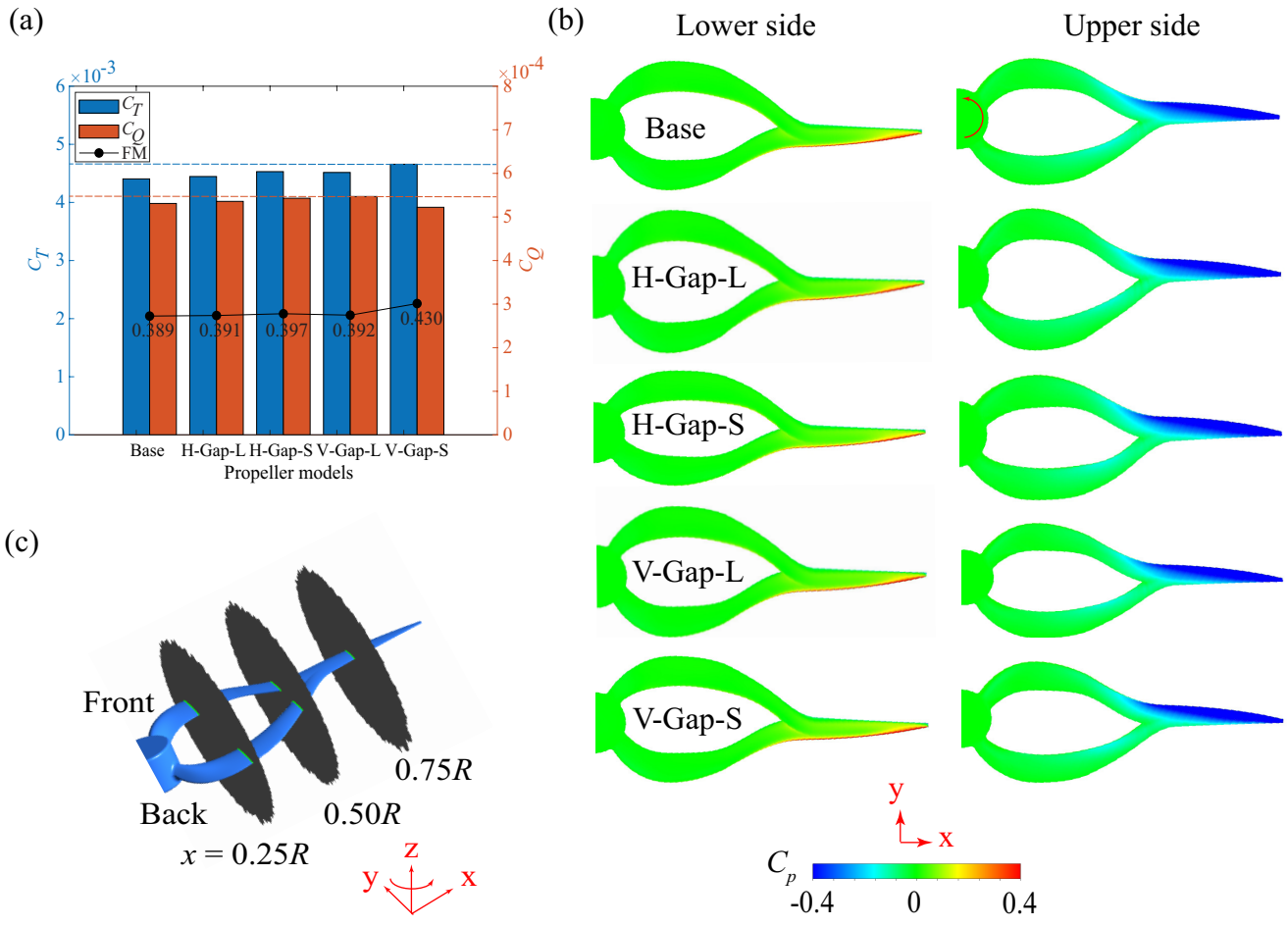


Figure 4. (**a**) Hybrid propeller performance comparison, (**b**) propeller surface pressure coefficient (C_p) contours, and (**c**) positions of clip planes for sectional analysis.

$$C_p = \frac{p}{\frac{1}{2}\rho U_{tip}^2}. \tag{17}$$

The pressure contours indicate significant variations on the upper side of the hybrid propellers, particularly near the intersection of the front and back blades within a single loop element. They also show that thrust is primarily generated by the outboard portion of the blade, with negative pressure on the upper surface and positive pressure on the lower surface.

To further examine the influence of spacing on performance, three radial locations ($0.25R$, $0.50R$, and $0.75R$, shown in Figure 4c) are selected for sectional analysis of C_p and C_f (skin-friction coefficient). The latter is defined in Equation (18), where τ_w is the wall shear stress:

$$C_f = \frac{\tau_w}{\frac{1}{2}\rho U_{tip}^2}. \tag{18}$$

Figure 5 presents both C_p (on the primary y-axis) and C_f (on the secondary y-axis). At $0.25R$ (Figure 5a), the flow from the front blade in the loop element favorably influences the static pressure distribution over the back blade and increases C_f near the leading and trailing edges. At $0.50R$ (Figure 5b), the opposite trend is observed: the flow from the front blade adversely affects only the upper surface of the back blade, reducing C_f on almost the entire blade surface. At both $0.25R$ and $0.50R$, the magnitudes of C_p and C_f are lower compared to $0.75R$. At $0.75R$ (Figure 5c), the V-Gap-S configuration exhibits the largest enclosed area in the C_p distribution, consistent with its highest thrust coefficient shown in Figure 4a. This supports the common practice of using measurements at $0.75R$ for thrust estimation in propeller studies. In terms of torque, V-Gap-S displays distinct changes in C_f at $0.25R$ and $0.50R$ compared to the other configurations. This suggests that geometry modifications within the inner 50% of the blade radius influence skin friction, thereby affecting torque generation.

5.2. Propeller Aeroacoustics

To investigate propeller aeroacoustics, thirteen receivers are positioned in the xz-plane at 15° interval, located six propeller radii from the origin, as shown in Figure 6a. For the primary tonal noise at BPF ($f^+ = 1$) in Figure 6b, all propellers exhibit a quadrupole-like directivity pattern, consistent with turbulent wake interactions and blade-tip vortex effects. The primary tonal noise reaches its maximum at approximately 30° and 150°, symmetric about the propeller axis. The largest variation, about 5 dB, occurs near 60° and 120°. At 90°, the H-Gap-L configuration does not exhibit the primary tonal noise (no peak at $f^+ = 1$); instead, it appears as part of the broadband noise and is therefore not considered. Because all propellers have the same disk area, the disk loading reduces to a function of thrust; thus, the differences in primary tonal noise among configurations can be primarily attributed to propeller thrust variation, where the V-Gap-S configuration has the largest thrust value.

In contrast, the broadband noise exhibits a dipole-shaped distribution (Figure 6c), indicating that it is mainly governed by flow turbulence. Among the tested configurations, H-Gap-S consistently produces the highest broadband noise levels, followed by V-Gap-S. This trend does not fully correlate with propeller torque, since V-Gap-L exhibits the largest torque coefficient (Figure 4a). It is important to note that a MATLAB built-in function with default settings was used to eliminate noise peaks in the sound pressure level (SPL) spectra. As discussed in Chen et al. [23], this approach may not remove all tonal peaks, leaving some residual contamination in the broadband noise. Supporting this, the SPL spectra at representative observer locations R1 (0°) and R7 (90°) are shown in Figure 6e and 6f,

respectively. Notably, at R7, the low-frequency range ($f^+ < 1$) indicates that the broadband noise of V-Gap-L is close to maximum, suggesting that broadband noise scales closely with propeller torque.

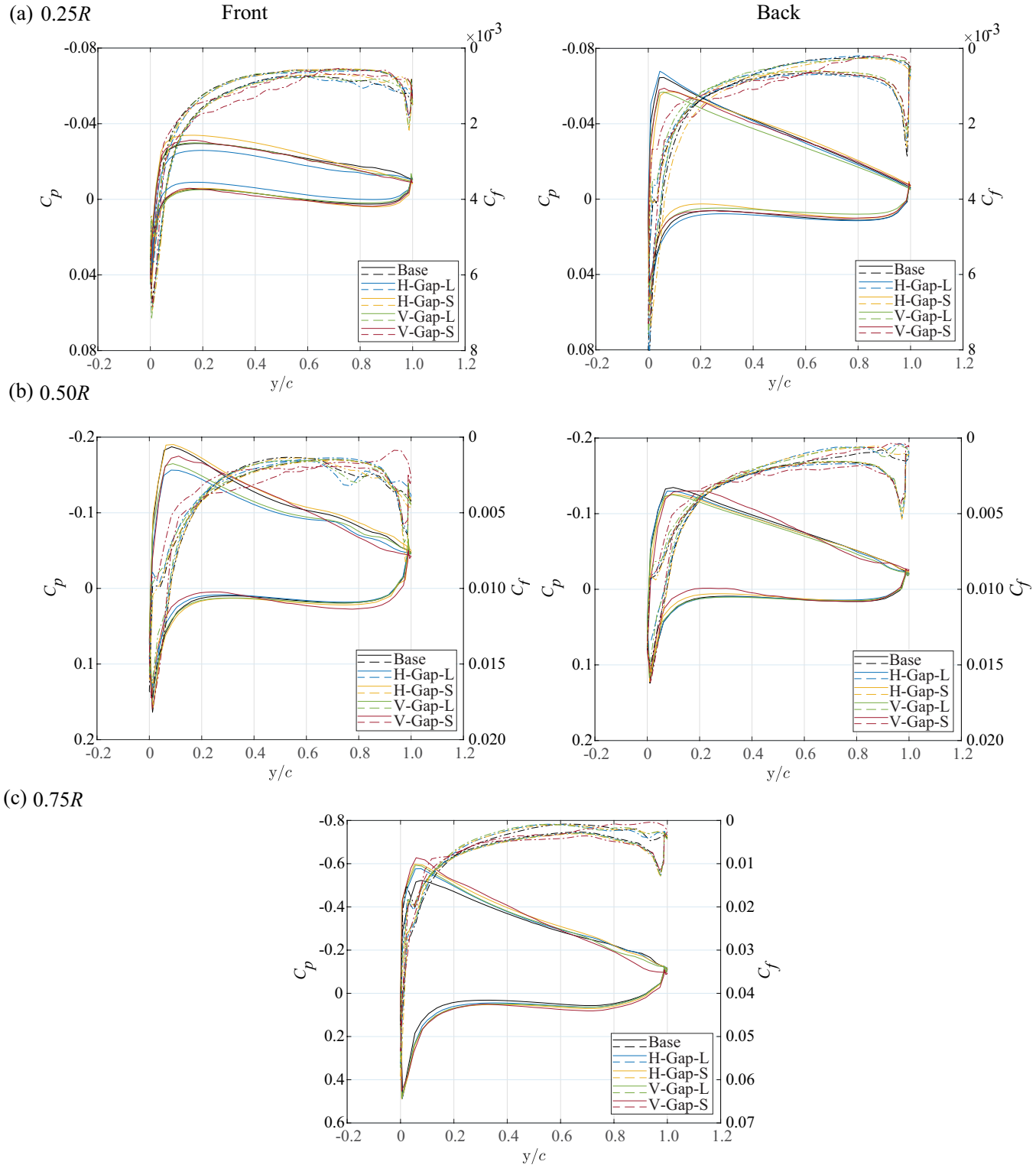


Figure 5. Comparison of static pressure coefficient (solid lines) and skin friction coefficient (dashed lines) on the blade surface at (**a**–**c**).

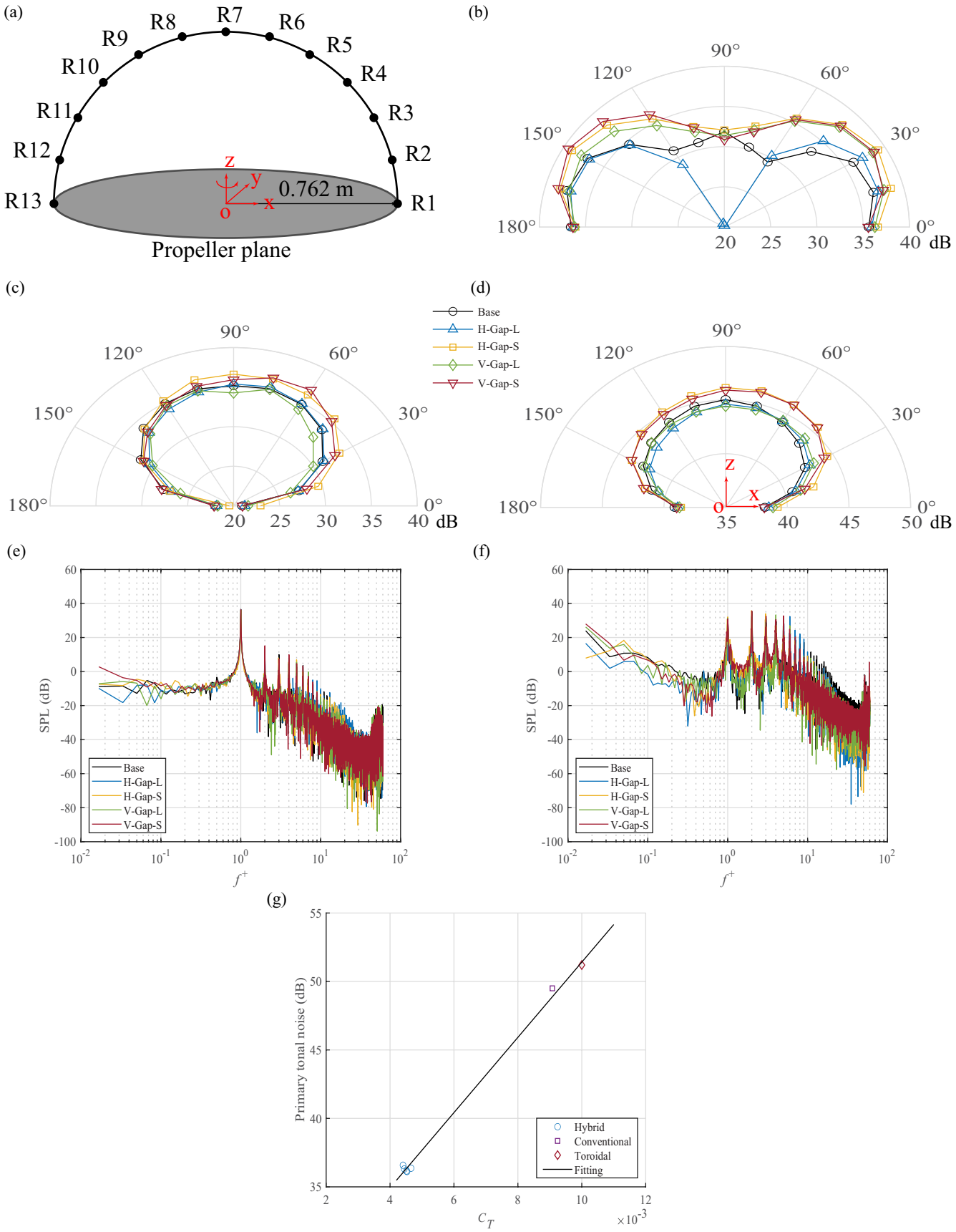


Figure 6. (**a**) Locations of 13 acoustic receivers, (**b**) primary tonal noise, (**c**) broadband noise, (**d**) OASPL, (**e**) SPL at receiver 1 (R1), (**f**) SPL at receiver 7 (R7), and (**g**) comparison of primary tonal noise at R1.

https://doi.org/10.3390/aerospace13010094

Finally, the overall sound pressure level (OASPL) directivity (Figure 6d) shows that H-Gap-S and V-Gap-S generates nearly identical OASPL values, while the remaining configurations cluster together with lower values. The maximum difference across all cases is about 1.5 dB. This variation implies that propeller FM influences the OASPL, since reduced propeller performance can lower OASPL. Taken together with the performance data in Sections 5.1 and 5.2, these results confirm that propeller aerodynamic performance strongly couples with acoustic signatures.

Consistent with this observation, previous studies on conventional [12] and toroidal propellers [23] have shown that the primary tonal noise measured at R1 increases approximately linearly with the thrust coefficient, C_T, as illustrated in Figure 6g. In those studies, primary tonal noise predictions from CFD were validated against experimental measurements conducted at identical rotational speed, rotation direction, propeller diameter, and blade number, showing good agreement. Based on these validated results, the primary tonal noise at R1 was not significantly influenced by electric motor noise in the experiments or by the selection of the transient ANSYS Fluent flow solvers. Consequently, drawing conclusions about noise reduction requires consistent performance conditions beyond simply holding RPM constant. Otherwise, an apparently quieter configuration may only reflect reduced propeller performance rather than true acoustic benefits.

5.3. Streamlines and TKE

To gain deeper insights into the flow characteristics, streamlines are visualized together with TKE (k) contours on three clip planes for each propeller configuration, as presented in Figure 7. TKE, a key parameter describing the intensity of velocity fluctuations associated with turbulent eddies, is nondimensionalized using Equation (19):

$$k/U_{tip}^2 = \frac{(\overline{u'u'} + \overline{v'v'} + \overline{w'w'})}{U_{tip}^2}, \tag{19}$$

where $\overline{u'u'}$, $\overline{v'v'}$, and $\overline{w'w'}$ represent the variances of the fluctuating velocity components, obtained statistically from the DDES computations. This nondimensionalization provides a consistent basis to compare turbulence levels across different propeller configurations and radial locations.

Among the five propeller configurations, the V-Gap-S configuration exhibits the lowest TKE levels across all three planes. At $0.25R$, turbulence generated by the front blade significantly impinges on the back blade in the base, H-Gap-L, and V-Gap-L configurations, largely due to the wider spacing that allows turbulent structures to affect the static pressure across the entire back blade surface, effectively acting as a turbulence generator that energizes the flow. At $0.50R$, the influence of the front blade turbulence is more localized; the smaller spacing in V-Gap-S limits turbulence to the top surface of the back blade, reducing its impact area. At $0.75R$, V-Gap-S alone maintains consistently low turbulence levels, correlating well with the performance trends observed in Figure 5.

Additionally, the streamlines provide qualitative insight into the local changes in angle of attack at $0.25R$ and $0.50R$, illustrating how the flow from the front blade interacts with the back blade. These observations help explain the differences in propeller performance among the various propeller configurations.

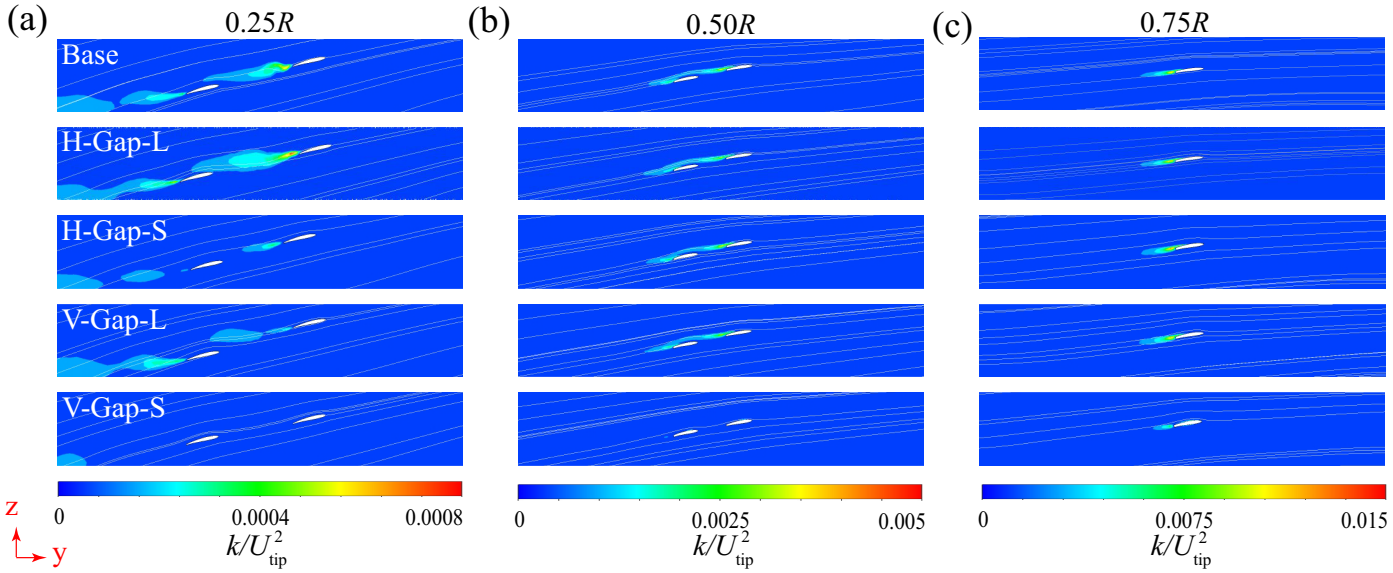


Figure 7. Streamlines and TKE contours at (**a**) 0.25*R*, (**b**) 0.50*R*, and (**c**) 0.75*R*.

5.4. Vorticity

To further investigate the underlying fluid mechanisms of spacing between loop elements on aerodynamics and aeroacoustics, Figure 8 visualizes the vortical structures surrounding the five propeller models. The Q-criterion, a widely used method for identifying vortex cores in a turbulent flow, is employed in its nondimensionalized form as shown in Equation (20):

$$Q_{norm} = \frac{Q_{raw} D^2}{U_{tip}^2}, \tag{20}$$

where Q_{raw} is obtained directly from ANSYS Fluent Simulations. The resulting Q-isosurfaces (Q_{norm} = 0.8) are colored by the normalized z vorticity, $\omega_z D/U_{tip}$, to provide additional insight into the rotational characteristics of the flow. Furthermore, the z vorticity distributions around the propellers are presented to capture the fluid's swirling motion and highlight regions of concentrated rotation.

From the top view in Figure 8, the blade tips are observed to interact strongly with tip vortices, particularly at the relatively low rotation speed of 3000 RPM. According to momentum theory, the vertical induced velocity in the propeller wake increases with rotational speed, which helps explain the aeroacoustic trends reported in Figure 6. Additionally, a vortex is observed to form and shed from the interaction between the front and rear blades around the mid-span region. The side view shows that, likely due to tip–vortex interaction, the tip vortices dissipate after approximately one revolution for all propeller models.

Closer inspection of the near-blade regions reveals subtle variations in vorticity above and below the blade tips. In particular, for the small-gap configurations (H-Gap-S and V-Gap-S), the changes on the z vorticity span a wider range. This suggests that the small-gap configurations amplify the aerodynamic influence of the front blade on the rear blade, increasing blade–air interactions and enhancing the effect of the mid-span vortex. These differences in vortical patterns provide a qualitative explanation for the observed variations in both propeller performance and noise levels across the different propeller configurations.

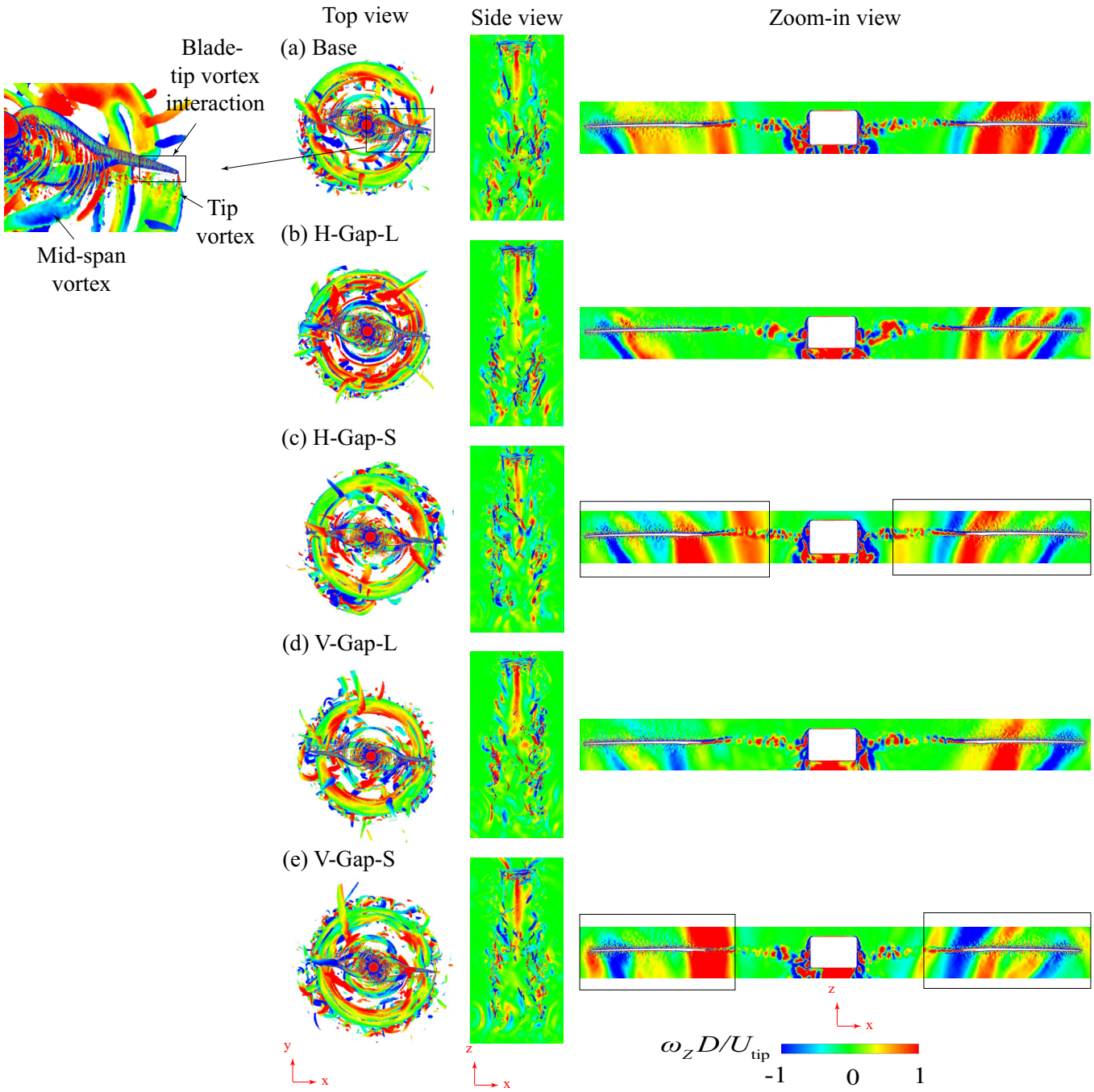


Figure 8. Top view of Iso-Q-surfaces (Q_{norm} = 0.8) (**left**), side view of Iso-Q-surfaces (**middle**), and z-vorticity near the blade surfaces (**right**): (**a**–**e**).

5.5. Time Derivative of Acoustic Pressure

To quantify the near-field flow fluctuations on propeller aeroacoustics, the time derivative of the acoustic pressure, dp'/dt, directly applied into Equation (10), is normalized as

$$C_{dp'/dt} = \frac{dp'/dt}{\frac{1}{2}\rho\frac{U_{tip}^3}{D}}. \tag{21}$$

The resulting contours are presented in Figure 9. The largest values of of dp'/dt occur occur near the leading edge at approximately the outbound of half blade. On the upper and lower surfaces of the blades, regions of positive and negative dp'/dt form quadrupole-like distributions, which are critical in understanding primary tonal noise. The only exception

is the H-Gap-L configuration, which shows no clearly defined pole on the lower surface in Figure 9b. The side views provide additional insight into the temporal pressure fluctuations in the near-tip region, where tip–vortex interaction is significant.

To examine radial trends, dp'/dt is extracted at three representative radial stations—0.25R, 0.50R, and 0.75R—and plotted in Figure 10. At 0.25R, the front blade exhibits relatively uniform dp'/dt for all propeller models, whereas the back blade shows significant variations near the leading edge, likely due to turbulence induced by the front blade. At 0.50R, the situation reverses: the front blade experiences larger dp'/dt fluctuations, while the back blade is less affected. At 0.75R, near the blade tip, the leading edge shows pronounced variations, with V-Gap-S exhibiting the largest changes, as indicated by the area enclosed by high dp'/dt values. The elevated time derivatives near the tip correspond to tip–vortex interactions, generating four primary "poles" around the tip surfaces that strongly influence both propeller performance and noise levels.

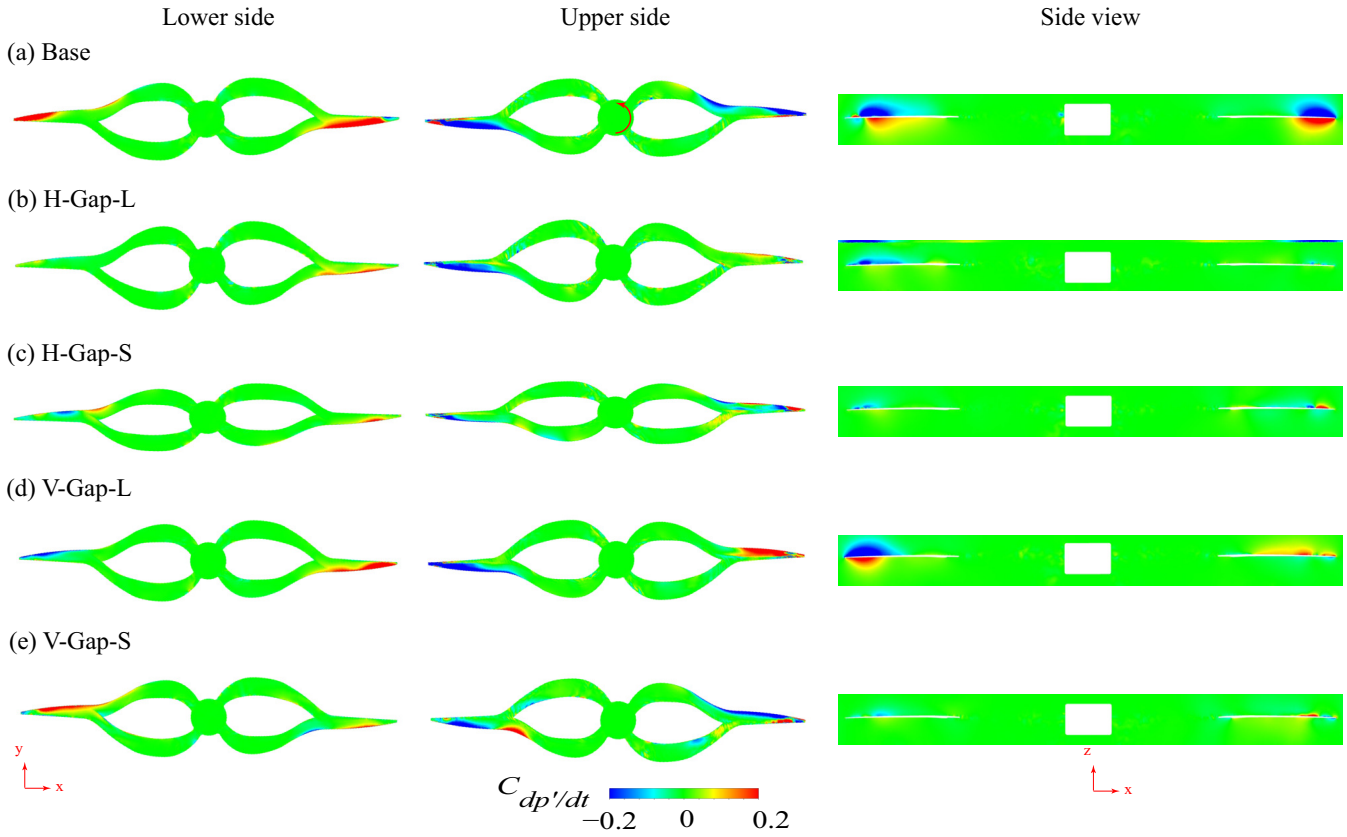


Figure 9. Time derivative of acoustic pressure contours on blade surfaces: lower side (**left**), upper side (**middle**), and near the blade surfaces (**right**): (**a**–**e**).

For regions away from the blade tips, the contributions of dp'/dt are primarily associated with broadband noise, as they reflect turbulence-induced pressure fluctuations. These observations provide a mechanistic explanation linking localized flow unsteadiness to overall propeller aeroacoustics, demonstrating how blade geometry and spacing modify the distribution of acoustic sources.

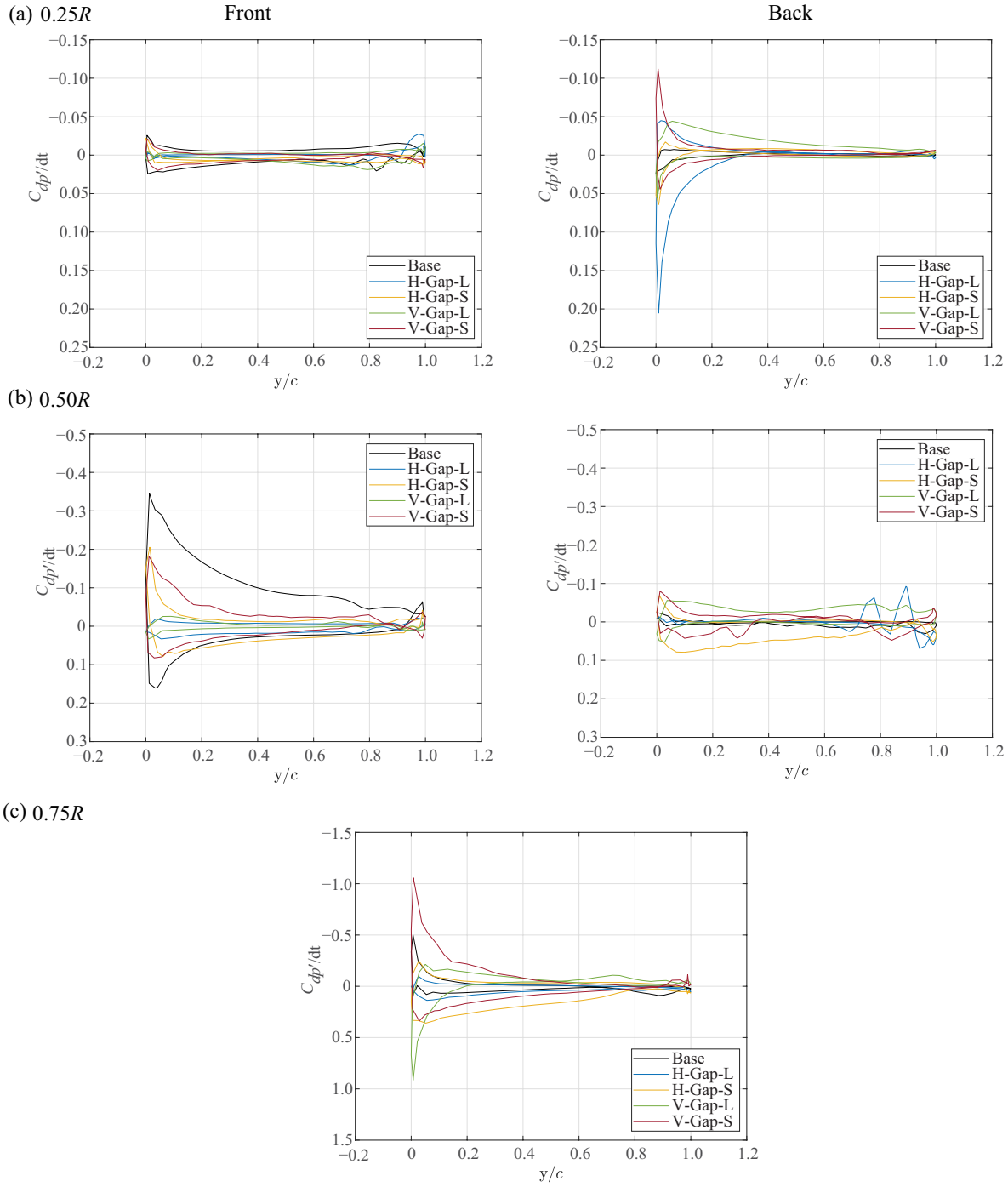


Figure 10. Comparison of time derivative of acoustic pressure on the blade surface at (**a**–**c**).

6. Conclusions

This study presents the first computational investigation of hybrid propellers that combine toroidal and conventional blade geometries. Five configurations—a baseline and four variants with modified loop-element spacing—were evaluated in terms of aerodynamic performance, aeroacoustic signatures, pressure-related parameters, and flow structures.

Among the tested designs, the V-Gap-S configuration provided the most favorable performance, achieving more than a 10% increase in FM relative to the baseline and maintaining the lowest turbulence kinetic energy across all radial stations. The analysis indicates that, due to the low rotation speed near the inner half of the blade, increasing

spacing in either the horizontal or vertical direction does not significantly impact propeller performance or aeroacoustics.

Aeroacoustic predictions demonstrated that primary tonal noise exhibits a quadrupole-like directivity pattern, with maxima at 30° and 150° associated with tip–vortex interactions. This noise component scales primarily with thrust, explaining the higher tonal radiation observed for the V-Gap-S configuration. In contrast, broadband noise displayed a dipole-shaped distribution dominated by turbulent flow, correlating with propeller torque. OASPL analysis showed a strong coupling between propeller performance and noise, with less efficient designs producing lower total noise levels.

Flow visualization and TKE analysis indicated that wider loop-element spacing allows turbulence generated by the front blade to impinge upon the rear blade, whereas reduced spacing primarily affects the top surface of the back blade. Examination of the time derivative of acoustic pressure highlighted the mechanisms behind the observed patterns in primary tonal noise, broadband noise, and OASPL. Tip–vortex interactions induce alternating positive and negative pressure change rates above and below the blade tips, particularly near the leading-edge regions.

Collectively, these findings confirm that propeller performance and aeroacoustics are inherently coupled. Blade geometry governs the interaction between aerodynamic loading and unsteady flow structures, which in turn shapes the noise signature. Importantly, these findings emphasize that assessments of noise reduction must consider matched-performance conditions, as quieter operation may otherwise arise from degraded aerodynamic performance rather than genuine acoustic improvements.

Author Contributions: Conceptualization, M.C. and T.F.; methodology, M.C.; investigation, M.C.; data curation, M.C.; writing—original draft preparation, M.C.; Software—J.E.; writing—review and editing, T.L., J.E. and T.F. All authors have read and agreed to the published version of the manuscript.

Funding: This research received no external funding.

Data Availability Statement: The raw data supporting the conclusions of this article will be made available by the corresponding author on request.

Conflicts of Interest: The authors declare no conflicts of interest.

Abbreviations

The following abbreviations are used in this manuscript:

BPF	Blade passing frequency
CFD	Computational fluid dynamics
DDES	Delayed detached eddy simulation
EASA	European Union Aviation Safety Agency
FAA	Federal Aviation Administration
FFT	Fast Fourier transform
FM	Figure of merit
FW–H	Ffowcs Williams and Hawkings
LES	Large eddy simulation
MIT	Massachusetts Institute of Technology
OASPL	Overall sound pressure level
RANS	Reynolds-averaged Navier–Stokes
RPM	Revolutions per minute
SPL	Sound pressure level
SST	Shear stress transport
TKE	Turbulence kinetic energy
UAM	Urban air mobility

References

1. Christian, A.; Cabell, R. Initial Investigation into the Psychoacoustic Properties of Small Unmanned Aerial System Noise. In Proceedings of the 23rd AIAA/CEAS Aeroacoustics Conference , Denver, CO, USA, 5–9 June 2017; AIAA Paper 2017-4051.
2. Bachmann, R.J.; Boria, F.J.; Vaidyanathan, R.; Ifju, P.G.; Quinn, R.D. A Biologically Inspired Micro-Vehicle Capable of Aerial and Terrestrial Locomotion. *Mech. Mach. Theory* **2009**, *44*, 513–526. [CrossRef]
3. Chen, M.; Hubner, J. Experimental and Analytical Analysis of Rotor-Wing Interaction in Hover for Low Reynolds Number Flow. *J. Aerosp. Eng.* **2021**, *34*, 04021073 . [CrossRef]
4. Chen, M.; Liu, L.; Chen, Y.; Wimsatt, J. Aeroacoustic and Aerodynamic Measurements at the Rotor Plane in the Interaction of a Small Rotor with Wings. *J. Acoust. Soc. Am.* **2024**, *156*, 2816–2826. [CrossRef] [PubMed]
5. Gojon, R.; Jardin, T.; Parisot-Dupuis, H. Experimental investigation of low Reynolds number rotor noise. *J. Acoust. Soc. Am.* **2021**, *149*, 3813–3829. [CrossRef] [PubMed]
6. Cattanei, A.; Ghio, R.; Bongiovı, A. Reduction of the tonal noise annoyance of axial flow fans by means of optimal blade spacing. *Appl. Acoust.* **2007**, *68*, 1323–1345. [CrossRef]
7. Leslie, A.; Wong, K.C.; Auld, D. Broadband noise reduction on a mini-UAV propeller. In Proceedings of the 14th AIAA/CEAS Aeroacoustics Conference (29th AIAA Aeroacoustics Conference), Vancouver, BC, Canada, 5–7 May 2008; AIAA Paper 2008-3069.
8. Wei, Y.; Xu, F.; Bian, S.; Kong, D. Experimental study of the performance of a propeller with trailing-edge serrations. *Acoust. Aust.* **2021**, *49*, 305–316. [CrossRef]
9. Lee, H.M.; Lu, Z.; Lim, K.M.; Xie, J.; Lee, H.P. Quieter propeller with serrated trailing edge. *Appl. Acoust.* **2019**, *146*, 227–236. [CrossRef]
10. Ning, Z.; Wlezein, R.; Hu, H. An experimental study on small UAV propellers with serrated trailing edges. In Proceedings of the 47th AIAA Fluid Dynamics Conference, Denver, CO, USA, 5–9 June 2017; AIAA Paper 2017-3813.
11. Hasegawa, M.; Sakaue, H. Propeller-noise reduction by microfiber coating on a blade surface. *Sens. Actuators A Phys.* **2024**, *371*, 115273. [CrossRef]
12. Chen, M.; Wimsatt, J.; Liu, M.; Fang, T. Experimental and Numerical Study of a UAV Propeller Printed in Clear Resin. *Aerospace* **2025**, *12*, 362. [CrossRef]
13. Sebastian, T.; Strem, C. Toroidal Propeller. U.S. Patent 10,836,466 B2, 17 November 2020.
14. Ion, G.; Simion, I. Performance of 3D Printed Conventional and Toroidal Propeller for Small Multirotor Drones. *J. Ind. Des. Eng. Graph.* **2023**, *18*, 27–32.
15. Žagar, L.; Jamšek, M. Comparison and Analysis of Toroidal and Classic Propellers. In Proceedings of the ERK'2023, Portorož, Slovenija, 28–29 September 2023; ERK paper 209-212.
16. Combey, K.; Chouiyakh, H.; Qaissi, K.; Faqir, M.; Elsayed, O. Aerodynamic Investigation of Novel Toroidal Joined Blade Tips Propeller. In Proceedings of the DICUAM 2024, Delft, The Netherlands, 22–24 March 2024.
17. Varun, S.; Jayarajan, N. Comparative Analysis of Toroidal Propeller and APC Propeller Performance for UAV using Computational Fluid Dynamics. In Proceedings of the IEEE International Conference on Interdisciplinary Approaches in Technology and Management for Social Innovation (IATMSI), Gwalior, India, 14–16 March 2024.
18. du Plessis, J.; Bouferrouk, A. Aerodynamic and Aeroacoustic Analysis of Looped Propeller Blades. In Proceedings of the 30th AIAA/CEAS Aeroacoustics Conference (2024), Rome, Italy, 4–7 June 2024; AIAA Paper 2024-3156.
19. du Plessis, J.; Bouferrouk, A.; Pontillo, A. Numerical Study of Noise Reduction on Looped Propeller Blades with Bio-inspired Tubercles. In Proceedings of the QuietDrones2024, Manchester, UK, 8–11 September 2024; QuietDrones conference paper 136.
20. Wei, W.; Ma, Y.; Wei, S.; Wang, D.; Guo, M.; Yan, Q. Analysis and Evaluation of Aerodynamic Noise Characteristics of Toroidal Propeller. *Drones* **2024**, *8*, 753. [CrossRef]
21. Shima, E.; Sun, J.; Liu, H.; Yonezawa, K.; Kaneko, H. Aeroacoustics, Psychoacoustics, and Aerodynamic Characteristics of Innovative Looped Propellers Using Catenary Curves. In Proceedings of the 30th AIAA/CEAS Aeroacoustics Conference (2024), Rome, Italy, 4–7 June 2024; AIAA Paper 2024-3111.
22. Li, P.; Liu, C.; Liu, Y.; Yang, Y. Multi-objective design and evaluation of a toroidal rotor for quadcopters. *Phys. Fluids* **2024**, *36*, 127165. [CrossRef]
23. Chen, M.; Liu, M.; Fang, T. Experimental and Numerical Analysis of a Toroidal Propeller. *J. Aerosp. Eng.* **2025**, *38*, 04025093. [CrossRef]
24. Malgoezar, A.M.; Vieira, A.; Snellen, M.; Simons, D.G.; Veldhuis, L.L. Experimental characterization of noise radiation from a ducted propeller of an unmanned aerial vehicle. *Int. J. Aeroacoust.* **2019**, *18*, 372–391. [CrossRef]
25. Guo, J.; Zhou, T.; Fang, Y.; Zhang, X. Experimental study on a compact lined circular duct for small-scale propeller noise reduction. *Appl. Acoust.* **2021**, *179*, 108062. [CrossRef]
26. Chen, M.; Chen, Y.; Hua, J.; Maier, N.; Burdette, D. Experimental Assessment of Blowing Effect on Vehicle Performance and Aero-acoustics in Small-Rotor/Wing Interaction. *J. Vib. Control* **2025**, *31*, 966–980. [CrossRef]
27. Pan, C.; Zhang, W. A comprehensive assessment on detached eddy simulation and delayed detached eddy simulation approaches in large-scale rotating separated flow in a centrifugal impeller under small flow rate. *Phys. Fluids* **2023**, *35*, 105111. [CrossRef]

28. Spalart, P.R.; Deck, S.; Shur, M.L.; Squires, K.D.; Strelets, M.K.; Travin, A. A New Version of Detached-eddy Simulation, Resistant to Ambiguous Grid Densities. *Theor. Comput. Fluid Dyn.* **2006**, *20*, 181–195. [CrossRef]
29. Menter, F.R. Two-Equation Eddy-Viscosity TurbulenceModels for Engineering Applications. *AIAA J.* **1994**, *32*, 1598–1605. [CrossRef]
30. Zhi, H.; Deng, S.; Chang, J.; Xiao, T.; Lu, Y. Pseudorotation Adjoint-Based Aerodynamic and Aeroacoustic Optimization Method for Isolated Rotors. *AIAA J.* **2025** , *63*, 2680–2694. [CrossRef]
31. Williams, J.F.; Hawkings, D.L. Sound generation by turbulence and surfaces in arbitrary motion. *Philos. Trans. R. Soc. Lond. Ser. A Math. Phys. Sci.* **1969**, *264*, 321–342. [CrossRef]
32. Chen, M.; Cranes, D.; Hubner, J.P. Experimental investigation of rotor-wing interaction at low disk loading and low Reynolds number. In Proceedings of the AIAA Aviation 2019 Forum, Dallas, TX, USA, 17–21 June 2019; AIAA Paper 2019-3034.
33. Johnson, W. *Rotorcraft Aeromechanics*, 1st ed.; Cambridge University Press: New York, NY, USA, 2013; p. 41.
34. Chen, M.; Hua, J.; Maier, N.; Burdette, D. Acoustic measurements in single-rotor/wing interaction at low disk loading and Reynolds number. *Int. J. Aeroacoust.* **2024**, *23*, 20–37. [CrossRef]

Disclaimer/Publisher's Note: The statements, opinions and data contained in all publications are solely those of the individual author(s) and contributor(s) and not of MDPI and/or the editor(s). MDPI and/or the editor(s) disclaim responsibility for any injury to people or property resulting from any ideas, methods, instructions or products referred to in the content.